# High-resolution imaging diagnosis of human fetal membrane by three-dimensional optical coherence tomography

Hugang Ren
Cecilia Avila
Cynthia Kaplan
Yingtian Pan

# High-resolution imaging diagnosis of human fetal membrane by three-dimensional optical coherence tomography

**Hugang Ren,[a] Cecilia Avila,[b] Cynthia Kaplan,[c] and Yingtian Pan[a]**
[a]Stony Brook University, Department of Biomedical Engineering, Stony Brook, New York 11794
[b]Stony Brook University, Department of Obstetrics, Gynecology, and Reproductive Medicine, Stony Brook, New York 11794
[c]Stony Brook University, Department of Pathology, Stony Brook, New York 11794

**Abstract.** Microscopic chorionic pseudocyst (MCP) arising in the chorion leave of the human fetal membrane (FM) is a clinical precursor for preeclampsia which may progress to fatal medical conditions (e.g., abortion) if left untreated. To examine the utility of three-dimensional (3D) optical coherence tomography (OCT) for noninvasive delineation of the morphology of human fetal membranes and early clinical detection of MCP, 60 human FM specimens were acquired from 10 different subjects undergoing term cesarean delivery for an *ex vivo* feasibility study. Our results showed that OCT was able to identify the four-layer architectures of human FMs consisting of high-scattering decidua vera (DV, average thickness $d_{DV} \approx 92 \pm 38\ \mu m$), low-scattering chorion and trophoblast (CT, $d_{CT} \approx 150 \pm 67\ \mu m$), high-scattering subepithelial amnion (A, $d_A \approx 95 \pm 36\ \mu m$), and low-scattering epithelium (E, $d_E \approx 29 \pm 8\ \mu m$). Importantly, 3D OCT was able to instantaneously detect MCPs (low scattering due to edema, fluid buildup, vasodilatation) and track (staging) their thicknesses $d_{MCP}$ ranging from 24 to 615 $\mu m$. It was also shown that high-frequency ultrasound was able to compliment OCT for detecting more advanced thicker MCPs (e.g., $d_{MCP} > 615\ \mu m$) because of its increased imaging depth. © *2011 Society of Photo-Optical Instrumentation Engineers (SPIE)*. [DOI: 10.1117/1.3646530]

Keywords: optical coherence tomography; high-frequency ultrasound; fetal membrane; microscopic chorionic pseudocyst; preeclampsia.

Paper 11142RRR received Mar. 22, 2011; revised manuscript received Sep. 12, 2011; accepted for publication Sep. 15, 2011; published online Oct. 26, 2011.

## 1 Introduction

Preeclampsia is a medical disorder associated with increased blood pressure and proteinuria during pregnancy or postpartum period.[1] It persists as a major cause of maternal and fetal mortality and morbidity in the United States and worldwide, affecting 5% to 8% of all pregnancies.[2] Preeclampsia may progress to eclampsia, which is potentially a fatal medical condition, thus rendering it crucial for clinical management.[3] Current diagnosis of preeclampsia mainly relies on clinical observation of the symptoms and other unspecific tests[4] (e.g., over 140/90 blood pressure or 300 mg protein in urine). However, these methods become effective only when preeclampsia develops to advanced stages. At that moment, the only treatment option is abortion or early delivery, which may lead to various medical complications to both the preterm newborn and the pregnant woman. Preeclampsia is a complicated syndrome that may exhibit different symptoms and no definite causative factors are found to be responsible for the disease.[5] Therefore, studies on specific features that have significant correlations with preeclampsia would be of great interest for providing an earlier, more accurate, and objective clinical diagnosis.

A recent study on fetal membranes (FMs) revealed that microscopic chorionic pseudocysts (MCP) arising in the chorion leave of the FMs were found to be strongly associated with preeclampsia ($p \leq 0.001$).[6,7] Although the results were based on an *ex vivo* FM specimen study and artifacts induced by pathological preparation (e.g., formalin fixation) could potentially be misinterpreted as MCP due to their similar appearances, the interesting finding that correlates MCP with preeclampsia may provide a new perspective in clinical prediction of preeclampsia. In this respect, an endoscopic imaging technique that enables instantaneous, noninvasive, or minimally invasive "optical biopsy" would be of high clinical relevance in the diagnosis of pathological conditions of pregnancy such as preeclampsia.

Among several emerging biomedical imaging techniques, optical coherence tomography (OCT) has shown great promise for noninvasive or minimally invasive optical biopsy of various subsurface tissue owing to its high resolution (e.g., 1 to 12 $\mu m$), intermediate imaging depth (e.g., 1 to 3 mm), and high detection sensitivity (e.g., over 100 dB dynamic range). Recent technological advances have enabled real-time two-dimensional (2D) and three-dimensional (3D) OCT imaging, Doppler OCT for functional subsurface blood flow imaging, ultrahigh-resolution OCT for subcellular imaging, and endoscopic OCT for noninvasive imaging of various internal organs.[8–10] Meanwhile, preclinical and clinical studies have demonstrated the utility of OCT in delineating morphological details of biological tissues (e.g., skin, oral cavity, esophagus, colon, bladder, and cervix),[11–13] and thus the potential for detecting cancers in these organs.

Address all correspondence to: Yingtian Pan, State University of New York at Stony Brook, Department of Biomedical Engineering, Bioengineering Building, Room G17, Stony Brook, New York 11794-5281. Tel: (631) 632-1519 (Office), (631) 632-1750 (Lab); Fax: (631) 632-2322; Email: yingtian.pan@sunysb.edu.

While our recent human study showed the clinical feasibility of our endoscopic OCT to significantly enhance early bladder cancer diagnosis,[10] here we present a pilot feasibility study on fresh human fetal membrane specimens from normal controls and from patients with MCP to explore the potential of OCT for early detection of pathological changes, which might serve in the prediction of preeclampsia or other diseases associated with pregnancy. We compare the image results of OCT and high-frequency ultrasound (HFUS) with the corresponding histological counterparts (clinical standard), so that the utility and potential limitations of OCT for high-resolution delineation of the morphology of human FMs and identification of pathological changes can be examined.

## 2 Materials and Methods

### 2.1 Sample Preparation

A 3D OCT imaging examination was performed on 60 human FM specimens. These specimens were acquired from 10 different subjects undergoing term cesarean delivery. For each subject, 6 samples were obtained from different sectors of the FMs, e.g., 4 from the posterior and anterior uterine wall and 2 near the cervix. The fresh human specimens were preserved in 0.9% saline, rinsed, stretched uniformly to the thickness closely mimicking the anatomic architecture of FMs *in vivo*, and then mounted on a custom $\phi 20$ mm ring holder placed in a modified ringer's buffer solution (37°C, $p$H 7.4) to undergo *ex vivo* imaging evaluations. All of the human specimen studies were approved by the Stony Brook University Institutional Review Board and with patients' prior informed consents.

### 2.2 3D OCT

Figure 1 depicts the schematic of the spectral-domain OCT (SDOCT) used to acquire all of the 3D images of the FM specimens in this study. The 3D OCT engine was upgraded from a high-speed 2D SDOCT setup previously reported,[10] in which a pigtailed broadband laser at central wavelength of $\lambda$ = 1310 nm and with a spectral bandwidth of $\Delta\lambda = 90$ nm (i.e., coherence length $L_c \approx 8.5$ $\mu$m) was used to illuminate a fiber optic Michelson interferometer. Green light from a laser diode
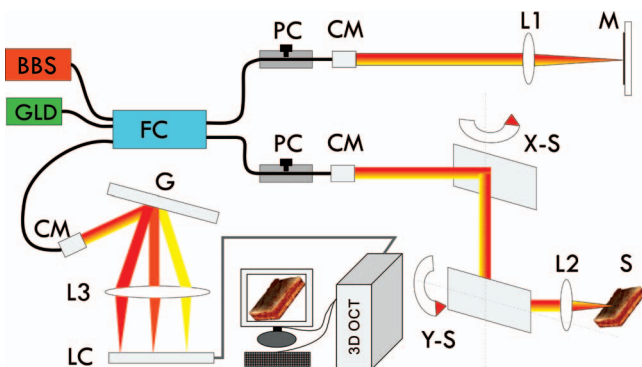


**Fig. 1** A sketch of the 3D OCT setup. BBS: broadband source; GLD: green diode laser; FC: fiber optic coupler; PC: polarization controller; CM: collimator; M: mirror; G: grating; LC: linear InGaAs camera; S: specimen (fetal membrane); X-S, Y-S: *X, Y* axes of the 2D servo scanner; L1–L3: lenses.

($\lambda = 532$ nm) was coupled into the fiber optic system for visual guidance of OCT scans. In the reference arm, a prism pair (e.g., using adjustable BK7 and fused silica wedge prisms) were used for dispersion compensation and a stationary retroreflective mirror was used to match the pathlength with the sample arm. The sample arm was connected to a handheld stereoscope in which light exiting the monomode fiber was collimated, scanned laterally by 2D servo mirrors (*x-y* scanners), and then focused by a near-infrared objective lens (*f* 40 mm/NA 0.12) onto the surface of the FM specimen under examination. Light from both reference and sample arms was recombined in the detection fiber and connected to a spectrometer in which the spectral interferograph was detected by a line InGaAs camera (1024×1 pixels, up to 47 kHz line rate) and interfaced via Camlink with a workstation for 2D and 3D image acquisition and reconstruction. Recent system development in detection optics and image acquisition and control resulted in enhanced axial and lateral resolutions (∼9 $\mu$m), large field of view (FOV: $5 \times 5 \times 2.5$ mm$^3$) at high dynamic range (>110 dB), and fast frame rate (8 to 47 fps).

### 2.3 Imaging Examination

With the FMs properly stretched and the maternal side facing upwards to mimic *in vivo* endoscopic imaging diagnosis, a number of 2D OCT prescans across the entire specimen were performed first to quickly locate the regions of interest (ROI). For each ROI, sequential OCT scans were performed within 60 s to acquire a 3D OCT image over a cubic volume of $5 \times 5 \times 2.5$ mm$^3$ and displayed in pseudo color to enhance visualization. By visual guidance with a green laser, the enface FOV for each 3D OCT image was landmarked to align the subsequent scans for 3D HFUS imaging,[14] which was acquired for some thickened specimens with advanced preeclampsia. 3D HFUS scans were performed using a miniature 40 MHz probe with an axial resolution of ∼40 $\mu$m (Vevo 770, Visualsonics Inc., Toronto, Canada). OCT delineates the morphological details (e.g., layers) of human FMs according to their backscattering differences. For simplicity, tissue backscattering was expressed by back reflectance, defined as the measured OCT intensity normalized to that of the top layer (i.e., decidua vera). Quantitative computer segmentation of FMs in both 2D and 3D OCT images was performed based on intensity gradient by adapting the algorithm previously reported,[12] and the average thickness (*d*) and back reflectance (*r*) of each layer were then analyzed. After the imaging study, the specimens were preserved in 10% formalin fixative together with the ring holders to avoid artifacts such as tissue deformation for hematoxylin and eosin (H&E) stained histological examination. A double blind histologic evaluation was independently performed by a clinical pathologist later to compare with the prior OCT and HFUS identifications and diagnoses. The data were presented as mean ± s.t.d.

## 3 Results

Previous studies have demonstrated the utility of OCT to enable high-resolution delineation of the morphological features of biological tissues (e.g., urinary bladder) based on their backscattering differences that attribute to the structural properties. Figure 2 exemplifies a typical cross-sectional 2D OCT image [Fig. 2(a)] of a normal FM acquired from the maternal side
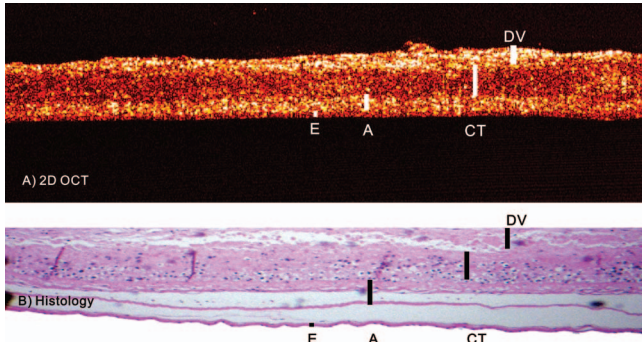
**Fig. 2** 2D images of a normal human fetal membrane. (a) cross-sectional OCT image; (b) corresponding H&E stained histology. DV: decidua vera ($d_{DV} \approx 92 \pm 38$ $\mu$m), CT: chorion and trophoblast ($d_{CT} \approx 150 \pm 67$ $\mu$m, $r_{CT/DV} = 0.51 \pm 0.17$), A: subepithelial amnion ($d_A \approx 95 \pm 36$ $\mu$m, $r_{A/DV} = 0.84 \pm 0.45$), and E: epithelium ($d_E \approx 29 \pm 8$ $\mu$m, $r_{E/DV} = 0.44 \pm 0.20$).

and the corresponding H&E stained histological evaluation [Fig. 2(b)]. OCT was able to identify the four layers of the FMs according to their backscattering differences. For instance, the outermost layer, decidua vera (DV) was relatively thin ($d_{DV} \approx 92 \pm 38$ $\mu$m), heterogeneous, and high scattering. The underlying chorion and trophoblast (CT) layer was thick ($d_{CT} \approx 150 \pm 67$ $\mu$m) and relatively low scattering ($r_{CT/DV} = 0.51 \pm 0.17$) possibly due to its loose structure and high interstitial fluid content. The subepithelial amnion (A) layer was slightly thinner ($d_A \approx 95 \pm 36$ $\mu$m) than the CT layer and was high scattering ($r_{A/DV} = 0.84 \pm 0.45$) resulting from subepithelial connective tissue. The innermost epithelium (E) was very thin ($d_E \approx 29 \pm 8$ $\mu$m or less, with 1 to 2 cell depths), uniform, and low scattering ($r_{E/DV} = 0.44 \pm 0.20$). It is noteworthy that the thicknesses of the intermediate amnion (A) and chorion (CT) layers and the FMs might vary with the trimester of pregnancy, the extent of tissue stretching, and the location of OCT scans, which might result in large error margins. Overall, the OCT identifications of the four layers within the FMs correlated well with the counterparts in the corresponding histological image [Fig. 2(b)] except detachment

of amnion in some specimens, which is a common artifact induced by tissue fixation during histological processing.

In addition to the 2D OCT presented in Fig. 2, 3D OCT image, e.g., by rendering 350 slices of sequential 2D cross-sectional OCT images, may provide improved image fidelity and more affirmative identifications of morphological features. For example, Fig. 3 summarizes the results of normal human FMs in which Fig. 3(e) shows a pie-cut graph of the 3D OCT image and Fig. 3(f) illustrates a 2D OCT slice with the four layers of the FMs automatically segmented based on their backscattering differences. Figures 3(a)–3(d) show the 3D images of the segmented 4 layers sequentially from DV and CT to A and E layers. Compared with 2D OCT in Fig. 2, 3D OCT in Fig. 3, owing to its improved spatial correlation (along the $y$-axis), provides enhanced image quality, which may permit more detailed analysis to characterize the architectural features of individual layers.

In this pilot human specimen study, not only normal human FMs but also potential pathological human FM specimens were examined to evaluate the utility of OCT for noninvasive and high-resolution imaging diagnosis of FM diseases (e.g., MCP). Figure 4 shows 2D OCT image [Fig. 4(a)] of an FM sample with MCP which was characterized by dark holes (low backreflection) with thickness of $d_{MCP} \approx 320$ $\mu$m between A and CT layers. The low-scattering characteristics of MCP (dark holes with $r_{MCP/DV} = 0.17 \pm 0.06$) were caused by fluid buildup (i.e., edema) within the lesions. Figure 4(b) represents the corresponding H&E histology which correlated well with the OCT identifications of the 4 layers and the cysts (MCP) within the CT and A layers except that the lesions ($d_{MCP} \approx 400$ $\mu$m) appeared larger than those ($d_{MCP} \approx 320$ $\mu$m) in OCT image [Fig. 4(a)]. This discrepancy likely resulted from the artifacts induced by tissue fixation and histological processing.

Similarly, Fig. 5 shows the results of 3D OCT of a human FM specimen with "early stage" MCP progression. Despite the fact that the surface image appeared normal, the segmented 3D OCT images revealed early, minor detachment ($d_{MCP} \approx 80$ $\mu$m, $r_{MCP/DV} = 0.14$) within the CT and A layers, resulting in drastically increased inhomogeneity within the CT layer [Fig. 5(c)]. Interestingly, the innermost epithelial layer E
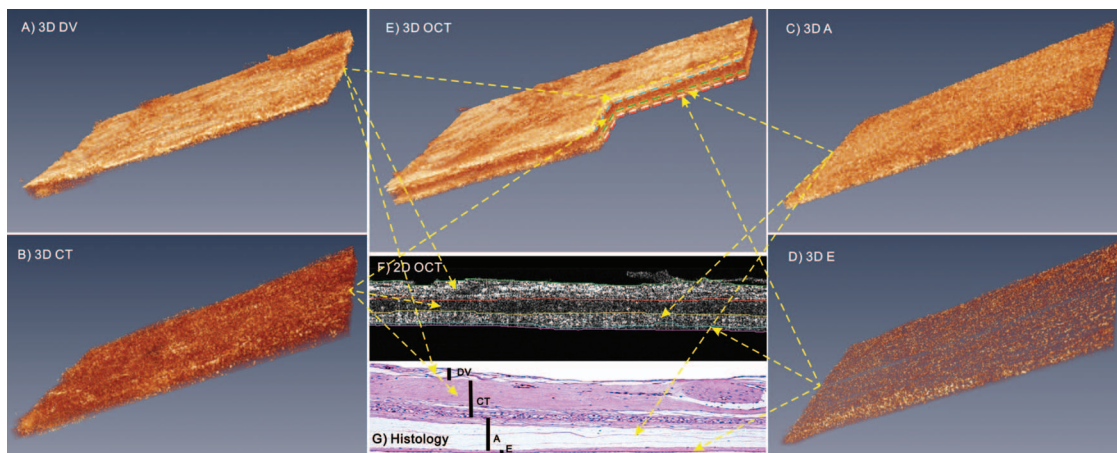


**Fig. 3** 3D image of a normal human FM. (a)–(d) 3D OCT images of the segmented DV, CT, A, and E layers; (e) 3D OCT image of the entire human FMs; (f) 2D OCT image to illustrate the automatic segmentation procedure based on the backscattering differences of each layer; (g) corresponding H&E histology of OCT image in (f).
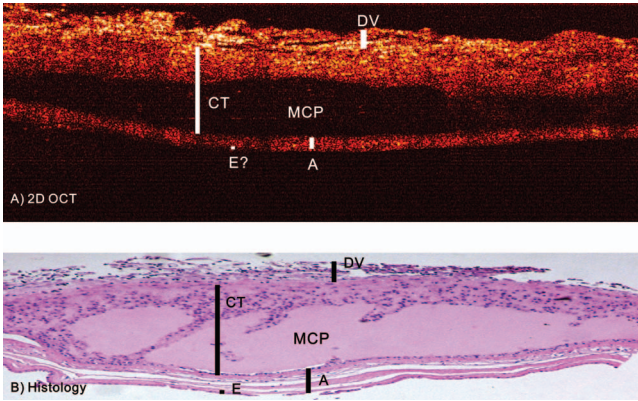
**Fig. 4** 2D image of a human FM specimen with MCP. (a) 2D OCT image; (b) corresponding H&E histology. The MCP lesions characterized by OCT as dark holes correlated with the cysts in histology. The thickness of MCP lesions in OCT ($d_{MCP} \approx 320~\mu$m) matched the histological counterpart ($d_{MCP} \approx 400~\mu$m).

[Fig. 5(a)] also became less uniform than the normal counterpart in Fig. 3(a), which could be associated with the inflammatory reactions of MCP. By detecting the size progression of MCP lesions, OCT was potentially capable of providing noninvasive evaluation (i.e., "staging") of MCP development and severity, in particular by 3D image segmentation to provide quantitative assessments of cyst depth (e.g., $d_{MCP} \approx 80~\mu$m in Fig. 5, $d_{MCP} \approx 320~\mu$m in Fig. 4) and the resultant inhomogeneity which was associated with fluid buildup, vasodilation, local microhemorrhage, macrophage, and mast cell accumulations. It should be noted that although the corresponding histological image in Fig. 5(g) correlated favorably with the OCT delineations, the artifacts induced by tissue fixation complicated the identification of MCP (cysts) from distortion (fall off) of CT and A layers, which might compromise the utility of histology for affirmative staging of MCP growth and spreading.

Figure 6 compares three human FM specimens to show the capability of OCT to assess the growth of MCP lesions.
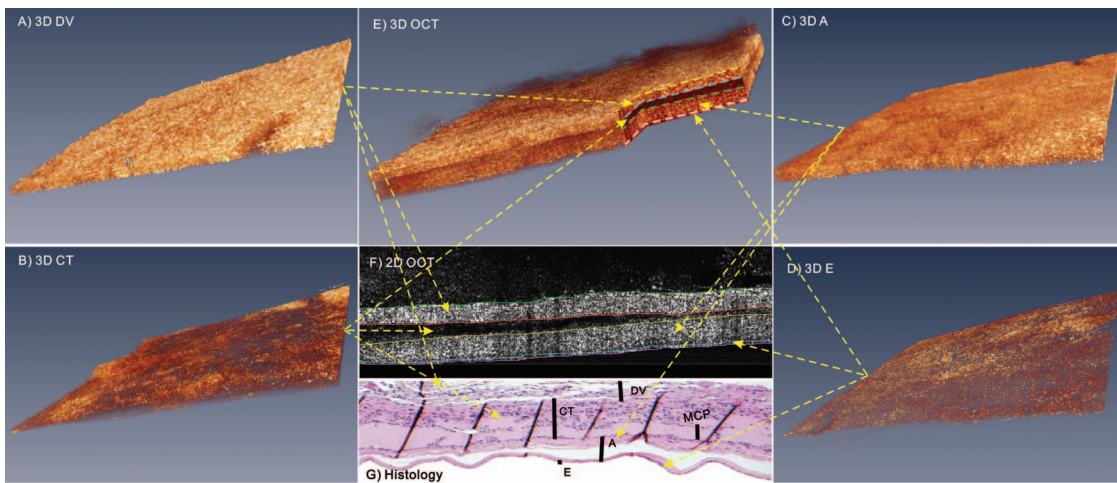


**Fig. 5** 3D OCT image of a human FM with MCP. (a)–(d) 3D OCT images of the segmented DV, CT, A, and E layers. (e) 3D OCT image of the intact human FMs with MCP; (f) segmented 2D OCT image to illustrate automatic segmentation based on their backscattering differences; (g) corresponding histology of the OCT image in (f). The CT and E layers were more heterogeneous than the previous normal specimen in Fig. 3.
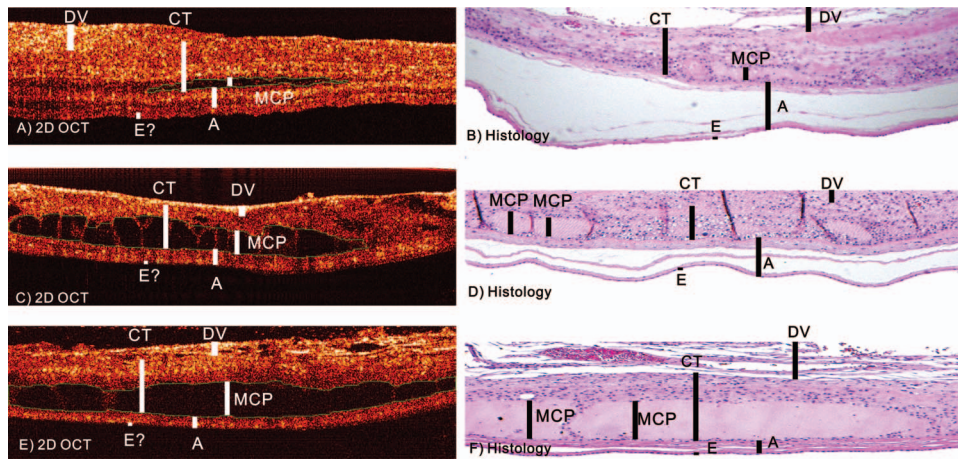


**Fig. 6** OCT images of human FM specimens with different-size MCP lesions compared with the corresponding H&E stained histological images. (a), (c), and (e) 2D OCT images with the MCPs automatically segmented as landmarked by green dashed circles. The thicknesses of MCPs were $d_{MCP} \approx 60~\mu$m (a), $d_{MCP} \approx 150~\mu$m (c), and $d_{MCP} \approx 265~\mu$m (e), respectively. The percentage areas of MCP, i.e., the ratios of the area of MCPs against the entire FM cross-section were 3.7% (a), 25.6% (c), and 28.3% (e). (b), (d), (f) The corresponding histological images. The thicknesses of MCPs were $d_{MCP} \approx 53~\mu$m (b), $d_{MCP} \approx 141~\mu$m (d), and $d_{MCP} \approx 251~\mu$m (f), which correlated with the OCT measurements despite artifacts such as tissue detachment induced by histological process.
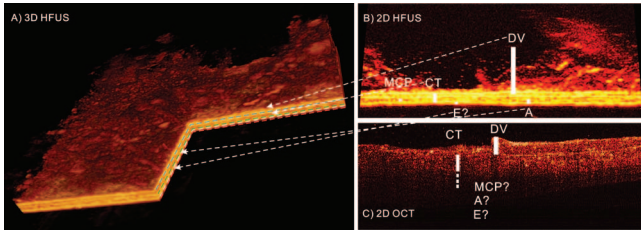
**Fig. 7** 3D HFUS image of a human FM with thick MCP. (a) 3D HFUS image; (b) a slice of 2D HFUS from image (a); (c) corresponding 2D OCT image. Despite the lower spatial resolution, HFUS was able to penetrate the entirety of the thicker FMs while the image depth of OCT was limited to layer DV or top CT.

Although the thickness of MCP ($d_{MCP}$) may vary with the point of measurement, the increase of MCP lesions could be differentiated by their mean thickness. OCT measurement of $d_{MCP} \approx 60~\mu$m, $r_{MCP/DV} = 0.13$ for the small MCP lesion in Fig. 6(a) correlated with the histological evaluation $d_{MCP} \approx 53~\mu$m in Fig. 6(b); the two large lesions $d_{MCP} \approx 150~\mu$m, $r_{MCP/DV} = 0.18$ [Fig. 6(c)] and, $d_{mcp} = 265$, $r_{mcp/dv} = 0.19$ [Fig. 6(e)] measured by OCT [Fig. 6(c)] were correlated favorably with the corresponding histological measures, $d_{MCP} \approx 141~\mu$m in Fig. 6(d) and $d_{MCP} \approx 251~\mu$m in Fig. 6(f), respectively. Alternatively, the percentage area of MCP lesion, i.e., $\Delta S_{MCP}(\%) = S_{MCP}/S_{FM}$ ($S_{MCP}$ and $S_{FM}$ are the cross-sectional areas of the PCM lesions and FMs) can be employed; the results of OCT measures were 3.7%, 25.6%, and 28.3% for Figs. 6(a), 6(c), and 6(e), respectively. In addition, we calculated the statistical result of the average thickness of MCP based on 32 lesions. The result showed that the MCP detectable by OCT varied from $d_{MCP} = 24~\mu$m to $d_{MCP} = 615~\mu$m with a mean thickness of 160 $\mu$m and a median thickness of 120 $\mu$m. These results suggest that endoscopic OCT could potentially be deployed to instantaneously diagnose MCPs and quantitatively evaluate (i.e., stage) their progress as well as the treatment effects. It is noteworthy from the histological images in Figs. 6(b), 6(d), and 6(f) that distortion and other artifacts (e.g., formalin infiltration) might compromise the evaluation of histological specimens.

The limited imaging depth of OCT (e.g., ∼1 to 3 mm) may potentially restrict its utility in the diagnosis and assessment of later-stage severe MCP lesions. For instance, for a few FM specimens (e.g., different locations on the FMs) with a thick DV layer (e.g., 2 to 4 mm) from the maternal side, OCT was unable to fully delineate the layered structures of the FMs, in particular, the innermost epithelium (E). In cases like this, HFUS might compliment OCT to overcome the imaging-depth limitation. To examine the feasibility, additional 3D HFUS scans following OCT imaging were performed using a miniature 40 MHz probe. Figure 7 exemplifies a 3D HFUS image of human FMs. The results show that because of lower resolution than OCT, the boundaries between the layers (e.g., DV, CT, and A) in HFUS images [Figs. 7(a) and 7(b)] were not as well defined than the counterparts in Figs. 2–5 and were unable to resolve the innermost epithelial layer (e.g., $d_E < 30~\mu$m). Nevertheless, the increased imaging depth of HFUS allowed it to visualize the full-thickness architecture of the thickened FMs. Interestingly, despite drastically reduced image contrast, HFUS was still able to detect the embedded intermediate-size MCP lesion. In contrast, due to markedly thicker ($d_{EV} > 1$ mm) DV layer and

drastically increased heterogeneity in this FM specimen, OCT was unable to delineate the underlying layers within the FMs.

## 4 Discussions and Conclusions

Early diagnosis of preeclampsia, crucial to effective therapeutic treatment, remains a clinical challenge due to the multifactorial nature of this disease.[4,5] A previous study revealed that MCP originating from the chorion leave (involving mostly CT and A layers) of the FMs was demonstrated to be closely related to preeclampsia ($p \leq 0.001$),[6] thus early diagnosis and evaluation of the progression of MCP could be of great clinical relevance. Current diagnosis is based on *ex vivo* histopathologic examination of the excised tissue specimens, whose clinical value is restricted by its invasive and destructive natures. Moreover, little has been studied about potential pathological misinterpretation of MCP as a result of artifacts induced by tissue fixation and processing.

In contrast, noninvasive early diagnosis of MCP could potentially benefit the treatment. Current medical imaging techniques such as MRI and ultrasound may provide limited diagnostic values because of their insufficient spatial resolution and other technical imperfections (e.g., potential radiation hazard to the fetus). OCT is an emerging optical imaging modality that, if integrated with endoscopy, permits noninvasive cross-sectional 2D and 3D imaging of biological tissue at high spatial resolutions (e.g., 1 to 10 $\mu$m) and over intermediate depths (e.g., 1 to 3 mm). Previous preclinical studies validated the capability of OCT for delineating the morphological details of various biological tissues such as oral cavity, bladder, esophagus, and cervix.[11–13] More interestingly, recent *in vivo* clinical studies clearly demonstrated the utility of our endoscopic OCT technique in significantly enhancing current clinical approach (i.e., white-light cystoscopy) for noninvasive diagnosis of early bladder cancer. Technically, the areas of fetal membranes prone to preeclamptic changes can potentially be imaged *in vivo* using our newly developed miniature (e.g., $\phi 2$ mm) flexible OCT catheter during intrauterine examination. We have presented a preliminary study based on human tissue specimens, including both normal control and diseased FMs. Results in Figs. 2 and 3 show that OCT was capable of delineating the morphological details of normal human FMs as the four layers (e.g., DV, CT, A, and E) based on their backscattering differences (e.g., $r_{CT/DV} = 0.51 \pm 0.17$; $r_{A/DV} = 0.84 \pm 0.45$; $r_{E/DV} = 0.44 \pm 0.20$). Results in Figs. 4 and 5 further demonstrate the utility of OCT to affirmatively detect the MCP lesions (cysts) in the CT layer of human FMs based on their drastically reduced backscattering (e.g., $r_{MCP/DV} = 0.17 \pm 0.06$). More importantly, by applying post-image processing techniques (e.g., image segmentation and registration) to the original 3D OCT image dataset, OCT morphometric placental analysis could potentially be implemented to provide quantitative, accurate evaluation of MCP progress (i.e., staging of MCP), which is essential to potentially monitor the preeclampsia development and to evaluate treatment effects. Our initial study using HFUS suggests that despite its limited spatial resolution to delineate layered structures in FMs, HFUS could be a complimentary method to detect large MCP lesions in markedly thickened FMs where a deeper penetration is needed. However, in order to further justify the utility and potential limitations of OCT and HFUS in the diagnosis of preeclampsia,

further detailed and more quantitative studies should be performed in the future, in particular, *in vivo* imaging evaluations.

In summary, we performed an *in vitro* study on fresh human FM specimens to examine the efficacy and limitations of OCT for future noninvasive or minimally invasive hysteroscopic OCT imaging of fetal membranes. Results presented above show that the high resolution and 3D imaging capability of OCT enabled delineation of morphological details of human FMs (e.g., DV, CT, A, and E layers) based on their backscattering differences, which correlated well with the corresponding histological evaluations. Additionally, OCT was able to identify early MCPs and accurately measure the size of these lesions. Further histomorphometric and immunohistochemical studies are needed to characterize the heterogeneity increases in these layers with the presence of different cell types and their accumulations so that more specific diagnosis of the severity and progress of MCP can be predicted. In addition, more *in vivo* animal and human studies will be required to fully examine the efficacy, technical feasibility, and safety of OCT hysteroscopy, as well as HFUS for potential future clinical application to minimally invasive diagnosis of MCP and staging their progress.

## Acknowledgments

## References

1. R. Gifford, P. August, G. Cunningham, L. Green, M. Lindheimer, D. McNellis, J. Roberts, B. Sibai, and S. Taler, "Report of the national high blood pressure education program working group on high blood pressure in pregnancy," *Am. J. Obstet. Gynecol.* **183**, 1–22 (2000).

2. B. Sibai, G. Dekker, and M. Kupferminc, "Pre-eclampsia," *The Lancet* **365**, 785–799 (2005).

3. L. Weinstein, "Syndrome of hemolysis, elevated liver enzymes, and low platelet count: a severe consequence of hypertension in pregnancy," *Obstet. Gynecol. Surv.* **142**, 159–167 (1982).

4. B. Sibai, "Diagnosis and management of gestational hypertension and preeclampsia," *Obstet. Gynecol.* **102**, 181–192 (2003).

5. R. Ness and J. Roberts, "Heterogeneous causes constituting the single syndrome of preeclampsia: a hypothesis and its implications," *Am. J. Obstet. Gynecol.* **175**, 1365–1370 (1996).

6. J. Stanek and E. Weng, "Microscopic chorionic pseudocysts in placental membranes: a histologic lesion of in utero hypoxia," *Pediatr. Dev. Pathol.* **10**, 192–198 (2007).

7. J. Stanek, "Diagnosing placental membrane hypoxic lesions increases the sensitivity of placental examination," *Arch. Pathol. Lab Med.* **134**, 989–995 (2010).

8. Z. Yuan, Z. Luo, H. Ren, C. Du, and Y. Pan, "A digital frequency ramping method for enhancing Doppler flow imaging in Fourier-domain optical coherence tomography," *Opt. Express* **17**, 3951–3963 (2009).

9. Z. Yuan, B. Chen, H. Ren, and Y. Pan, "On the possibility of time-lapse ultrahigh-resolution optical coherence tomography for bladder cancer grading," *J. Biomed. Opt.* **1**, 050502 (2009).

10. H. Ren, W. Waltzer, R. Bhalla, J. Liu, Z. Yuan, C. Lee, F. Darras, D. Schulsinger, H. Adler, and J. Kim, "Diagnosis of bladder cancer with microelectromechanical systems-based cystoscopic optical coherence tomography," *Urology* **74**, 1351–1357 (2009).

11. D. Adler, C. Zhou, T. Tsai, J. Schmitt, Q. Huang, H. Mashimo, and J. Fujimoto, "Three-dimensional endomicroscopy of the human colon using optical coherence tomography," *Opt. Express* **17**, 784–796 (2009).

12. H. Ren, Z. Yuan, W. Waltzer, K. Shroyer, and Y. Pan, "Enhancing detection of bladder carcinoma in situ by 3-dimensional optical coherence tomography," *J. Urology* **184**, 1499–1506 (2010).

13. C. Pitris, P. Hsiung, X. Li, W. Drexler, J. G. Fujimoto, A. Goodman, and M. Brezinski, "*In vivo* cervical imaging with an integrated optical coherence tomography colposcope," in *Biomedical Optical Spectroscopy and Diagnostics*, T. Li, ed., Vol. 38 of OSA Trends in Optics and Photonics (Optical Society of America, 2000), paper SuC5.

14. Z. Yuan, Z. Wang, R. Pan, J. Liu, H. Cohen, and Y. Pan, "High-resolution imaging diagnosis and staging of bladder cancer: comparison between optical coherence tomography and high-frequency ultrasound," *J. Biomed. Opt.* **13**, 054007 (2008).